Electronic Supplementary Material (ESI) for Energy & Environmental Science.

## Supporting Information

# Rechargeable Aqueous $Zn^{2+}$-Battery with High Power Density and Long Cycle-life

Fei Wang,‡[a,b] Enyuan Hu, ‡ [c] Wei Sun, ‡[a] Tao Gao, [a] Xiao Ji,[a] Xiulin Fan, [a] Fudong Han, [a] Xiao-Qing Yang,*[c] Kang Xu* [b] and Chunsheng Wang* [a]

a. Department of Chemical and Biomolecular Engineering, University of Maryland, College Park , MD 20742 , USA
b. Electrochemistry Branch, Sensor and Electron Devices Directorate, Power and Energy Division, U.S. Army Research Laboratory, Adelphi, MD 20783, USA.
c. Chemistry Division, Brookhaven National Laboratory, Upton, NY 11973, USA

## Experimental Section

### Synthesis of $Li_3V_2(PO_4)_3$@C

$NH_4VO_3$, $NH_4H_2PO_4$, LiOH and ascorbic acid were purchased from Sigma-Aldrich. The molar ratio of Li:V:P was 3.06:2.00:3.00. The $NH_4VO_3$, $NH_4H_2PO_4$, LiOH, 20 % excess ascorbic acid and glucose were add to the distilled water under vigorous stirring at 60$^o$C. The mixed solution was spray-dried to obtain the precursor powders. Afterward, the precursor were first heated at 350$^o$C for 4h and calcined at 700$^o$C for 10h under Ar atmosphere.

### Synthesis of $LiV_2(PO_4)_3$

The $LiV_2(PO4)_3$ was prepared by electrochemical method through extracting two Li from the $Li_3V_2(PO4)_3$ in the 4 m $Zn(OTf)_2$ electrolyte with Zn as both counter and reference electrodes. The upper cut-off voltage was set to 1.9 V vs Zn.

### Materials Characterizations

The morphology of the sample was investigated by scanning electron microscopy (SEM, Hitachi SU-70) and transmission electron microscopy (TEM, JEM 2100 FEG, 200 keV). X-ray diffraction (XRD) patterns were obtained on Bruker Smart 1000 (Bruker AXS, Inc.) using Cu Kα radiation with an airtight holder from Bruker. *In situ* XRD experiment was performed at 17BM beamline of the Advanced Photon Sources (APS) at Argonne National Laboratory (ANL) using a Perkin Elmer amorphous-Si flat panel detector. The *in situ* cell is made by assembling active material, carbon black and PTFE binder into a plastic pouch. The pouch cell is then sandwiched by two metallic plates with carbon window in the center which guarantees the pressure on the cell. Collected raw image data was then integrated to yield the 2theta-intensity XRD pattern using software Fit2D[1]. X-ray absorption spectroscopy (XAS) measurements were performed at 12BM beamline of the Advanced Photon Sources (APS) at Argonne National Laboratory (ANL) in the transmission mode. The X-ray absorption near edge structure (XANES) and Extended X-ray absorption fine structure (EXAFS) spectra were processed using the Athena software package[2]. The samples for XANES spectroscopy were recovered from full aqueous battery in 2032 coin cell configuration after electrochemical cycling. The samples were washed by DME three times and then dried under vacuum for two hours. The AUTOBK code was used to normalize the absorption coefficient, and separate the EXAFS signal, $\chi(k)$, from the isolate atom-absorption background. The extracted EXAFS signal, $\chi(k)$, was weighted by $k^3$ to emphasize the high-energy oscillations and then Fourier-transformed in a $k$ range from 3.0 to 12.5 Å$^{-1}$ to analyze the data in R space.

**Electrochemical Measurements**

The electrodes were fabricated by compressing active materials, carbon black, and polytetrafluoroethylene (PTFE) at weight ratio of 8:1:1 onto the titanium grid. Zinc trifluoromethanesulfonate ($Zn(OTf)_2$)) was purchased from TCI. The aqueous Zn-ion electrolyte was prepared by dissolving 4 mol $Zn(OTf)_2$ into 1 kg $H_2O$. The three-electrode devices for electrodes consist of $Li_3V_2(PO_4)_3$@C as working, active carbon as the counter and Ag/AgCl as the reference electrodes. Cyclic voltammetry (CV) was carried out using CHI 600E electrochemical work station. EIS were obtained by an electrochemistry work station (Gamry Interface3000) over a frequency range from 1 MHz to 0.01 Hz, with an AC amplitude of 10 mV. The full cell was assembled in CR2032-type coin cell. The charge-discharge experiments were performed on a Land BT2000 battery test system (Wuhan, China) at room-temperature. To get the average potential, the total energy was divided by the maximum capacity. The total energy was calculated by integrating the cell voltage vs. capacity curve. We have added the explanation into the supplement part.

**DFT calculations.**

All DFT calculations were performed with the spin-polarized generalized gradient approximation (GGA) within the Perdew-Burke-Ernzerhof (PBE) functional.[3] A plane-wave basis set and the Projector Augmented Wave (PAW) method were used which are implemented in the Vienna ab initio simulation package (VASP).[4,5] The Hubbard parameters (GGA+U) were used to correct the incomplete cancelation of the self-interaction of the GGA.[6] An effective U-value of 3.2 eV for V ion were used. A plane-wave basis set with energy cutoff of 520 eV and 2 x 2 x 2 Monkhorst-Pack k point meshes were used to ensure that the total energies converged to less than 0.1 meV. The calculated reaction free energy neglected the entropic contributions.

**AIMD calculations**.

The *ab initio* molecular dynamics (AIMD) simulations in this study were performed using the VASP package.[7] A minimal Γ-centered 1 x 1 x 1 k-point grid was used. The AIMD simulations were performed on $LiZn_{0.25}V_2(PO_4)_3$ structure. The time step of molecular dynamics was chosen to be 2 fs. The procedure of the AIMD simulations is as follows: i) At the beginning of the MD simulations, the $LiZn_{0.25}V_2(PO_4)_3$ samples are assigned an initial temperature of 100 K according to a Boltzmann distribution. ii) The $LiZn_{0.25}V_2(PO_4)_3$ samples are then heated up to the desired temperature (873K, 1073K, 1273K, 1573K) by velocity scaling over 1000 time steps (2 ps), and then equilibrated at the equilibrium temperature for 5000 time steps (10 ps) in the ensemble with a constant volume and with a Nosé–Hoover thermostat. iii) The MD simulations for diffusion are then performed for 40 ps in the NVT ensemble.

The diffusion coefficient is defined as the mean square displacement (MSD) over time:

$$D = \lim_{t\to\infty} \frac{\langle [r(t)]^2 \rangle}{6t}$$

The average mean square displacement $\langle [r(t)]^2 \rangle$ was calculated as:

$$\langle [r(t)]^2 \rangle = \frac{1}{N}\sum_i \langle [r_i(t+t_0)]^2 - [r_i(t_0)]^2 \rangle$$

Where $r_i(t)$ is the displacement of the *i*-th Li ion at time *t*. The calculated displacement $r_i(t)$ is the displacement of an individual Li atom. And *N* is the total number of ion in the system. The coefficient is finally attained from the slope of the average MSD vs. time plot for each temperature, from which an Arrhenius plot is obtained which yielded the activation energy.

The lithium ionic probability densities were calculated from the atom trajectories monitored during the AIMD simulations. The ionic probability density values within a structure were calculated by subdividing the supercell into a grid mesh with an edge length of 0.5 Å and counting the number of time steps for which each cell is occupied by a Li ion. The MSD, activation energy and ionic probability densities were calculated by pymatgen and the structural matching results were visualized using VESTA in this study. [8,9]

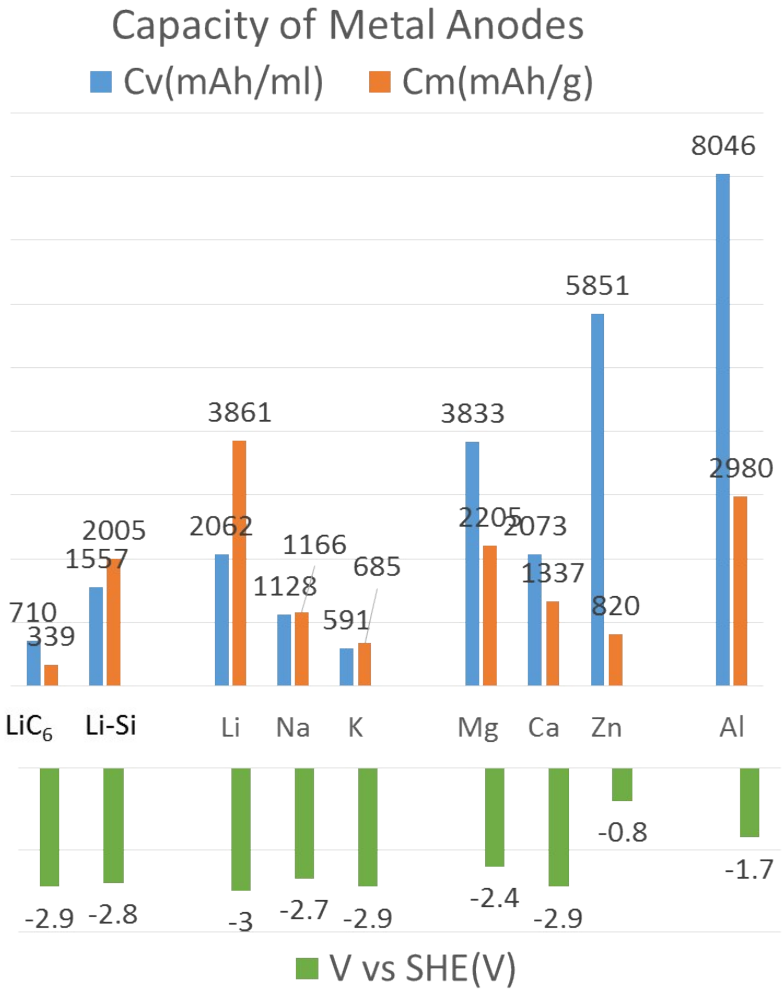

**Figure S1.** The gravimetric and volumetric capacities of different metal anodes.

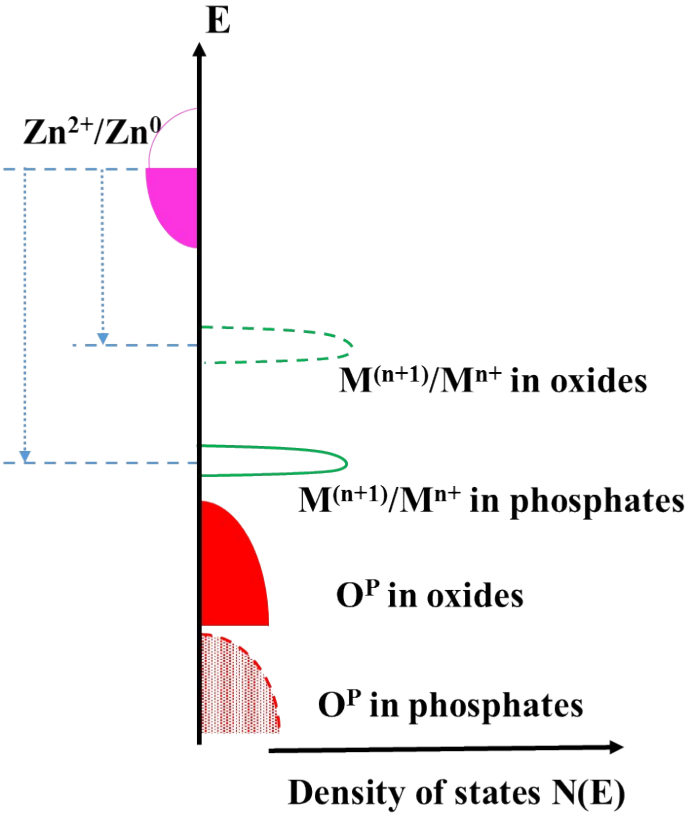

**Figure S2.** Schematic of the corresponding energy vs density of states showing the relative positions of the Fermi energy in an itinerant electron band for a $M^{(n+1)}/M^{n+}$ redox couple relative to zinc in oxides and phosphates.

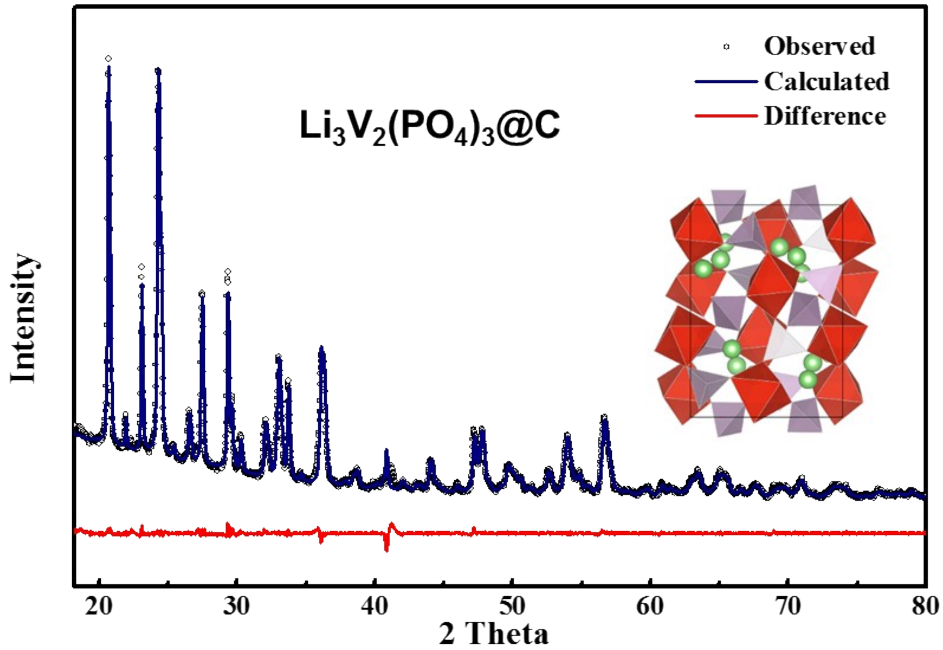

**Figure S3.** (b) Powder XRD pattern of $Li_3V_2(PO_4)_3$ and its Rietveld refinement results

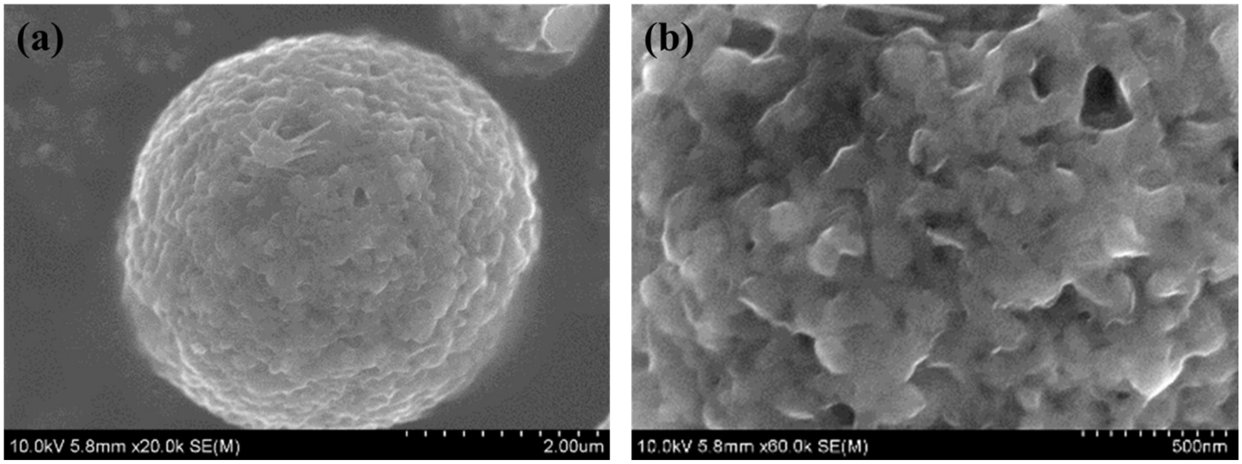

**Figure S4.** Scanning electron microscopy (SEM) image of the $Li_3V_2(PO_4)_3$@C

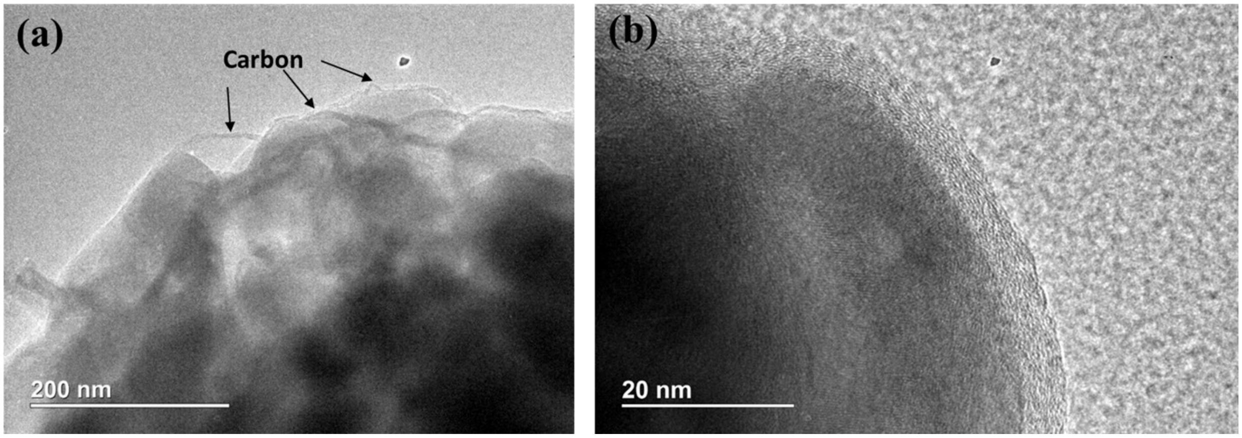

**Figure S5.** Transmission electron microscopy (TEM) image of the $Li_3V_2(PO_4)_3$@C

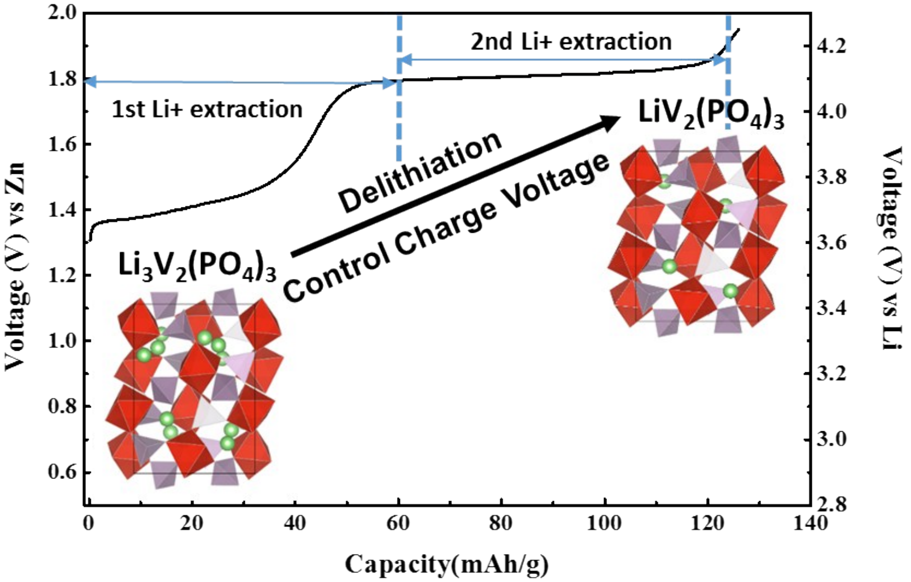

**Figure S6.** The electrochemical preparation of the $LiV_2(PO4)_3$ by extracting two Li from the $Li_3V_2(PO4)_3$ in the 4 m $Zn(OTf)_2$ electrolyte with Zn as both counter and reference electrodes.

Monoclinic $Li_3V_2(PO_4)_3$ contains three fourfold crystallographic positions for lithium in the framework of metal octahedron and phosphate tetrahedron sharing oxygen vertices. As has been intensively reported, the extraction of three distinct Li-ions from the $Li_3V_2(PO_4)_3$ depends on the charging voltage. In the monoclinic $Li_3V_2(PO_4)_3$, the extraction of the first 0.5 $Li^+$ occurs at 3.65V (vs Li), which is associated with the presence of an ordered Li phase of intermediate composition $Li_{2.5}V_2(PO_4)_3$. Then the extraction of the second 0.5 $Li^+$ occurs at 3.75 V (vs Li), relating to the removal of Li–ions from the stable tetrahedral sites to form the $Li_2V_2(PO_4)_3$. The second $Li^+$ extraction happens at 4.1V (vs Li), due to the change of the $V^{3+}/V^{4+}$ redox couple to the $V^{4+/5+}$ redox couple, and leads to the formation of the $LiV_2(PO_4)_3$. So, the formation of the $LiV_2(PO_4)_3$ could be achieved by controlling the charging voltage.

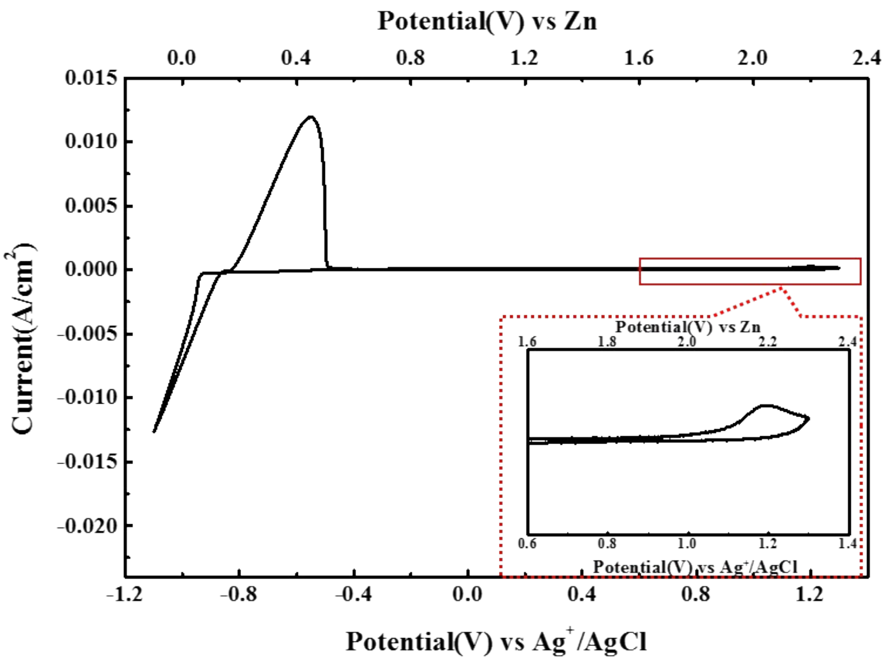

**Figure S7.** The electrochemical stability window of the 4 m $Zn(OTf)_2$ electrolyte.

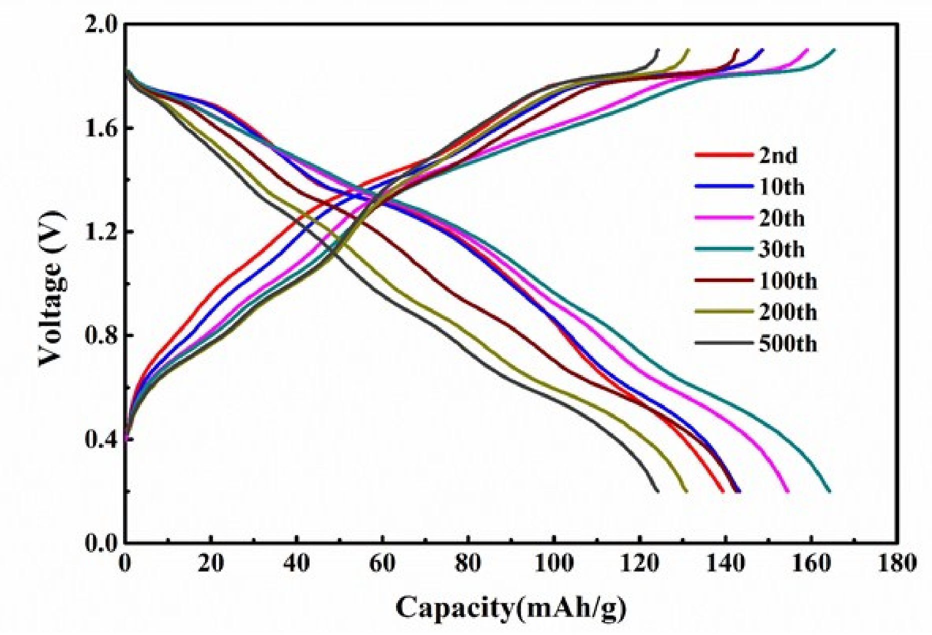

**Figure S8.** The typical voltage profiles of $LiV_2(PO_4)_3$ at different cycles between 0.2 V and 1.9 V in the 4 m $Zn(OTf)_2$ electrolyte at the current density of 2 C (1 C: 150 mA/g, electrode areal mass loading: 10 mg/cm$^2$).

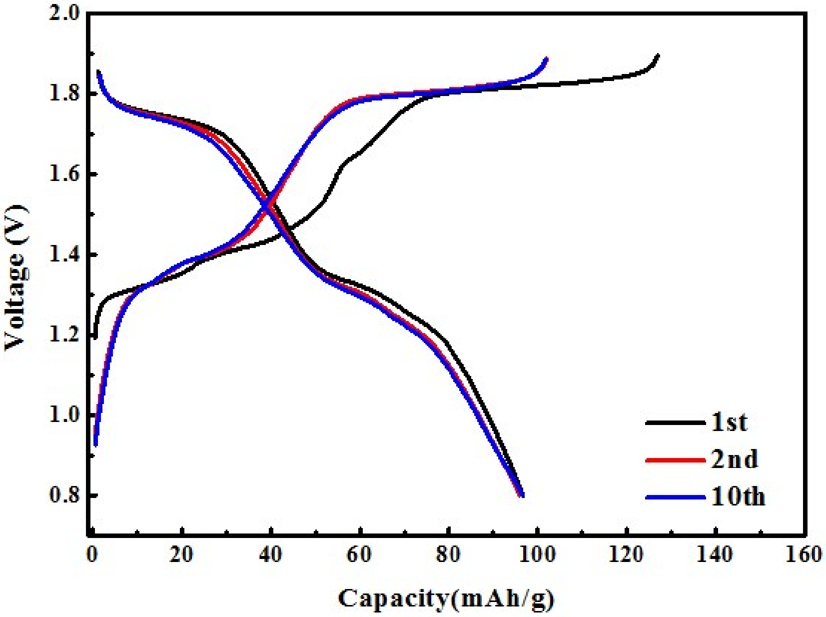

**Figure S9.** The typical voltage profile of $LiV_2(PO_4)_3$ between 0.8 V and 1.9 V in the 4m $Zn(OTf)_2$ electrolyte in the ambient temperature at the current density of 2 C (1 C: 90 mA/g, electrode areal mass loading: 8 mg/cm$^2$).

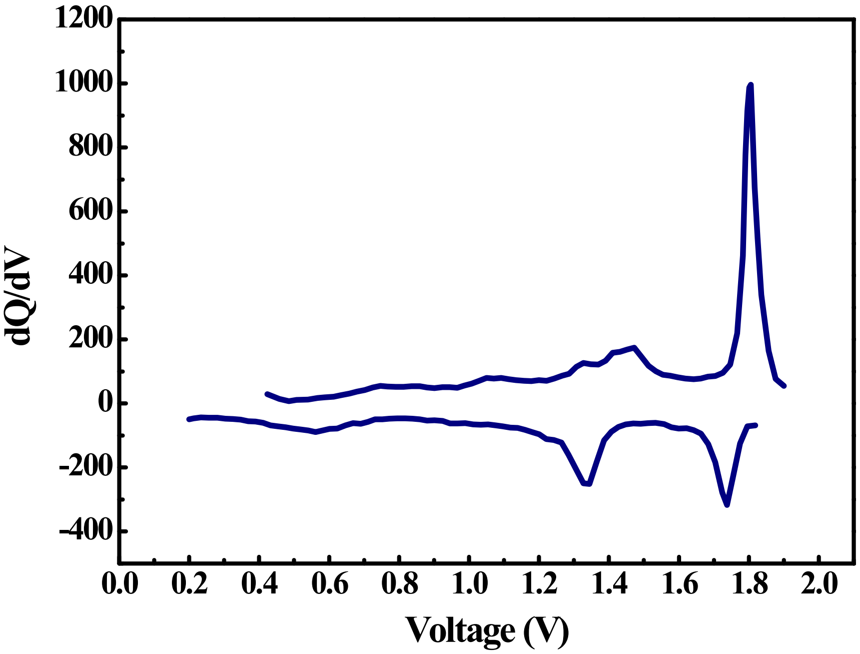

Figure S10. The differential capacity vs. voltage (dQ/dV) curves of the 1$^{st}$ cycle.

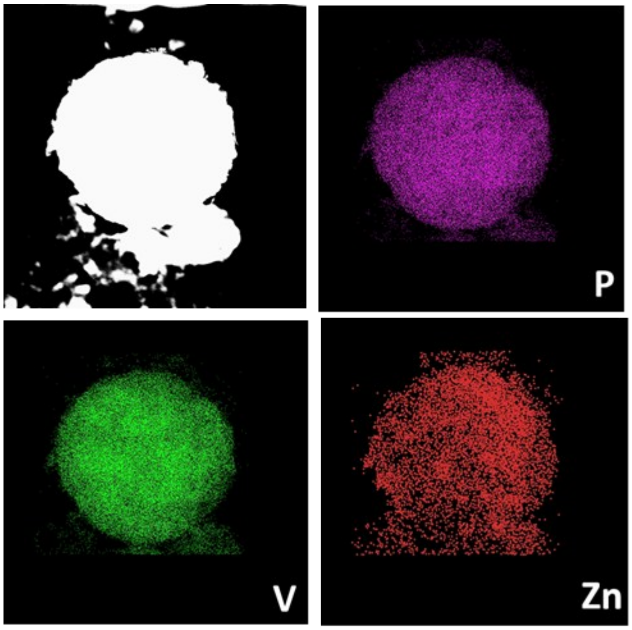

Figure S11. TEM element mapping of the $LiV_2(PO_4)_3$ discharged to 0.2 V.

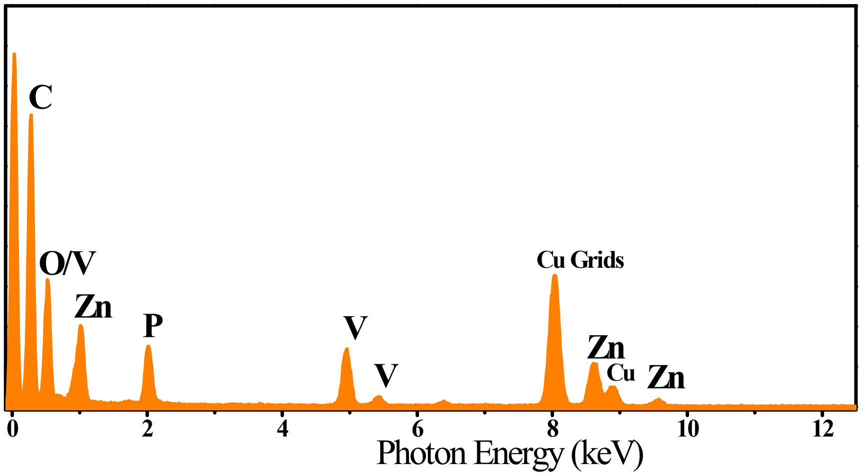

**Figure S12.** The EDX elemental analysis of the $LiV_2(PO_4)_3$ discharged to 0.2 V.

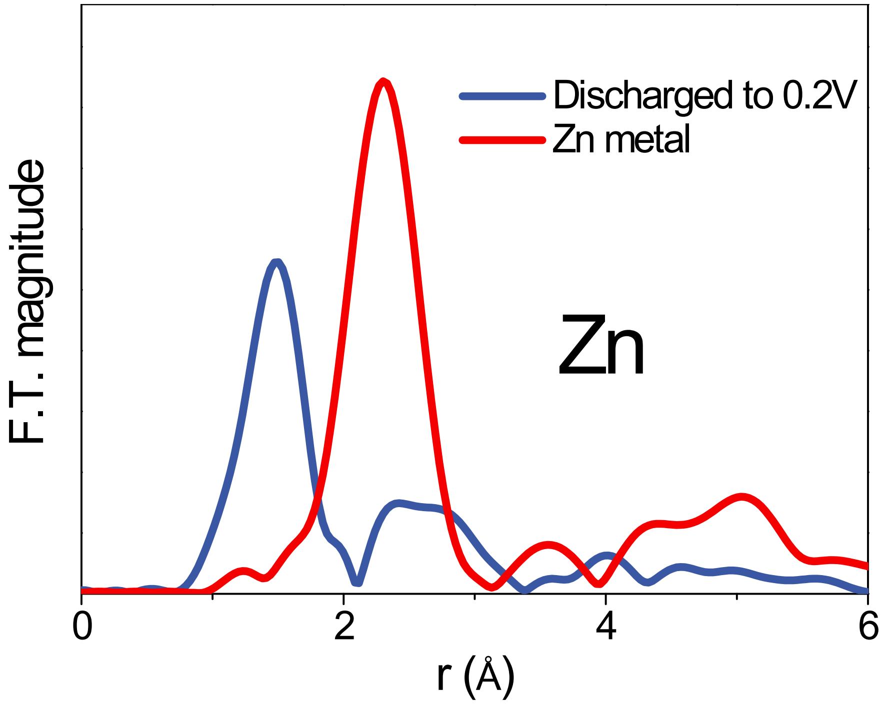

**Figure S13.** Fourier-transformed EXAFS spectra collected at the Zinc K-edge of the $LiV_2(PO_4)_3$ electrode discharged to 0.8 V

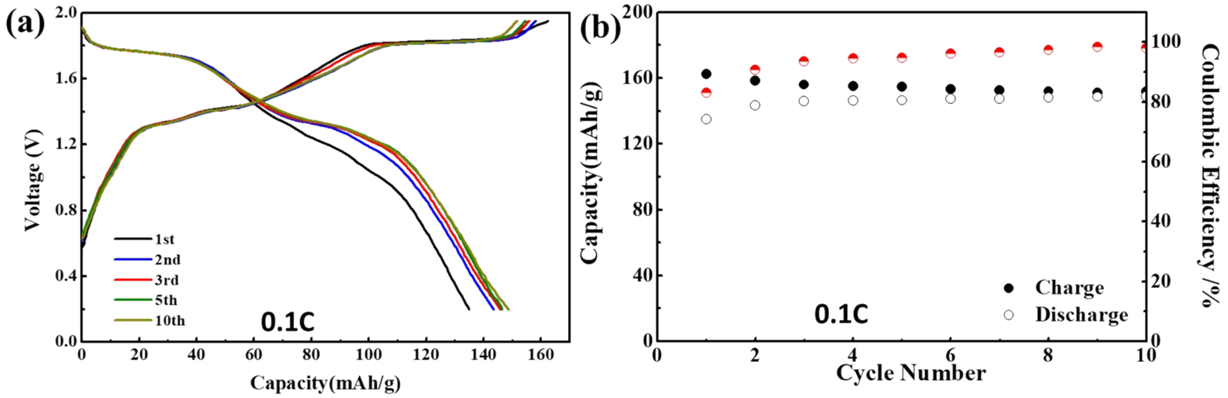

**Figure S14.** The typical voltage profile and cycling performance of $LiV_2(PO_4)_3$ between 0.8 V and 1.9 V in the 4m $Zn(OTf)_2$ electrolyte in the ambient temperature at the current density of 0.1 C.

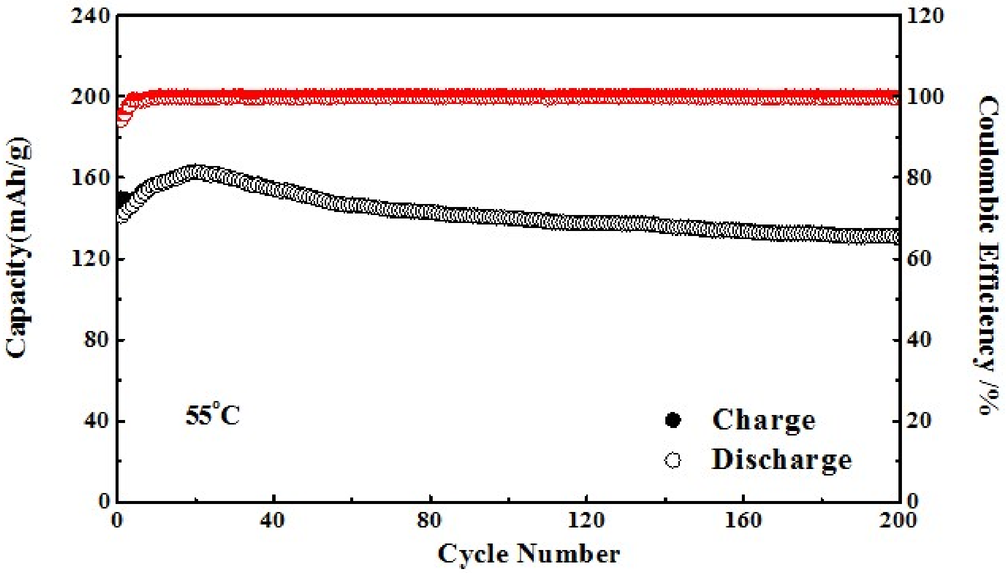

**Figure S15.** The cycling performance and the corresponding coulombic efficiency at the rate of 2 C at 55°C.

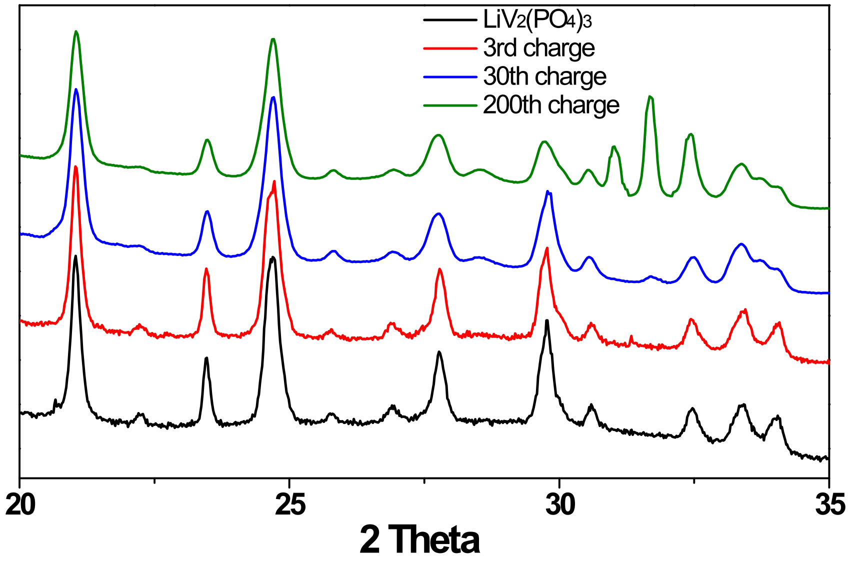

**Figure S16**. The XRD patterns of the LiV2(PO4)3 electrodes after different cycles.

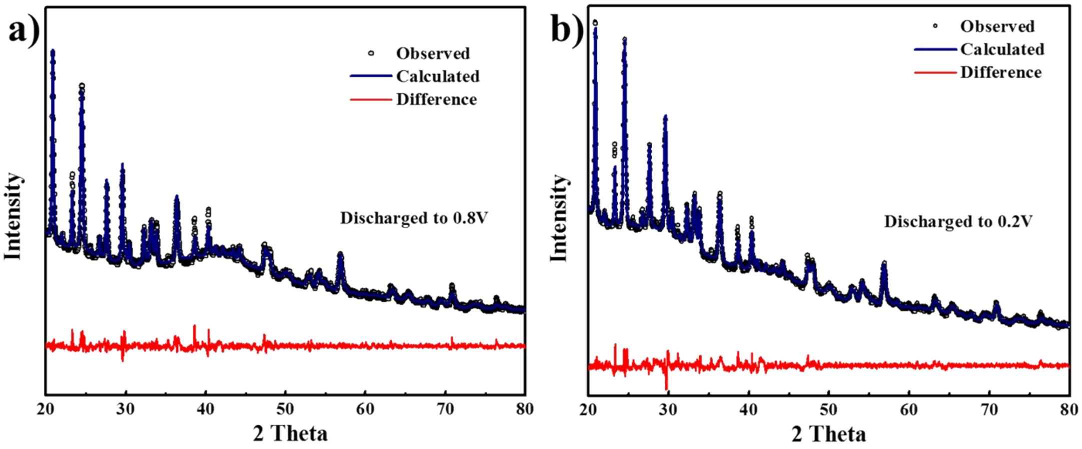

**Figure S17.** The XRD pattern and its Rietveld refinement results of the $LiV_2(PO_4)_3$@C electrode at the different discharge states.

|  | a(Å) | b(Å) | c(Å) | B(deg) | V |
|---|---|---|---|---|---|
| **$Li_3V_2(PO_4)_3$** | **8.6197** | **8.6158** | **12.063** | **90.4437** | **895.839** |
| **$LiV_2(PO_4)_3$** | **8.4718** | **8.5254** | **11.6607** | **91.4587** | **841.927** |
| **0.8V** | **8.5267** | **8.5726** | **11.9075** | **90.6289** | **870.338** |
| **0.2V** | **8.5402** | **8.5746** | **12.0605** | **90.5539** | **883.135** |
| **1.9V** | **8.4968** | **8.4647** | **11.9512** | **91.2013** | **859.378** |

**Table S1.** Crystallographic Data for different charge state.

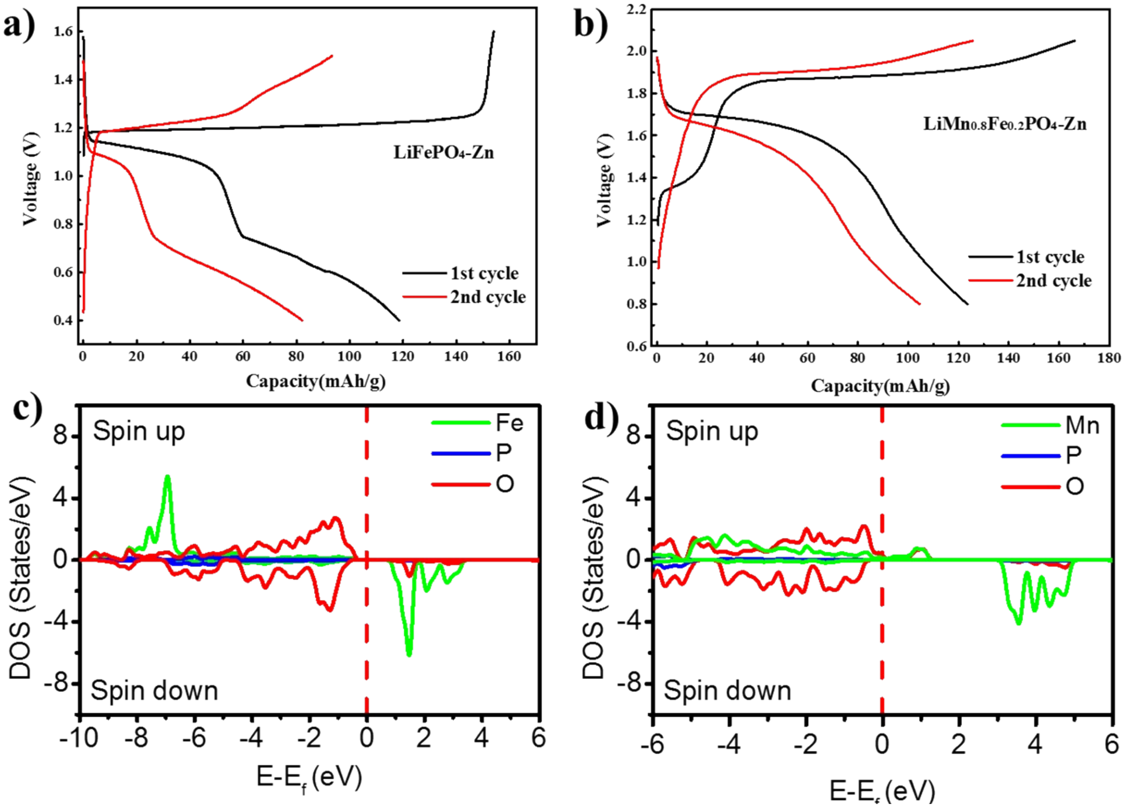

**Figure S18.** a) The typical voltage profile of $LiFePO_4$ in the 4m $Zn(OTf)_2$ electrolyte at the current density of 100 mA/g. b) The typical voltage profile of $LiMn_{0.8}Fe_{0.2}PO_4$ in the 4m $Zn(OTf)_2$ electrolyte at the current density of 100 mA/g. c)The DOS for the de-lithiated $LiFePO_4$. d) The DOS for the de-lithiated $LiMn_{0.8}Fe_{0.2}PO_4$.

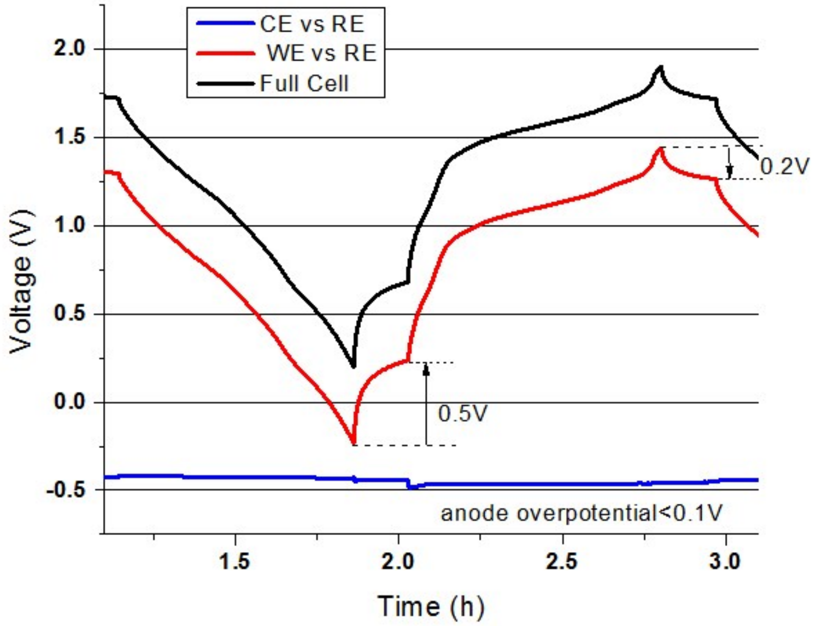

**Figure S19.** The potential of Zn anode (CE) and $LiV_2(PO_4)_3$ cathode (WE) vs. Zn Reference electrode (RE) in a three-electrode set-up and the full cell voltage in a full cycle.

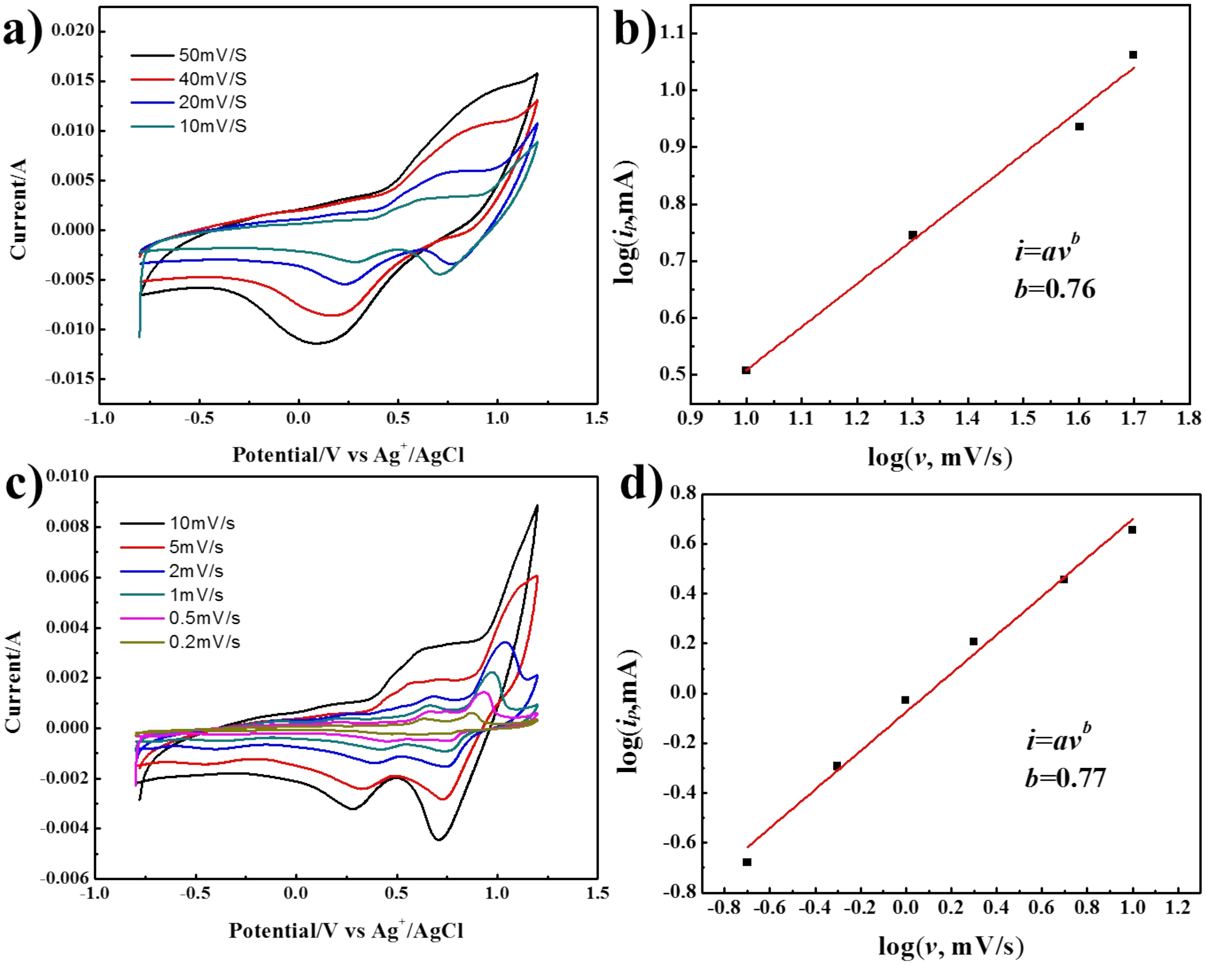

**Figure S20.** CV curves at different sweep rates ($v$) and corresponding log $i_p$ versus log $v$ of the $LiV_2(PO_4)_3$ electrode in the 4 m $Zn(OTf)_2$ electrolyte.

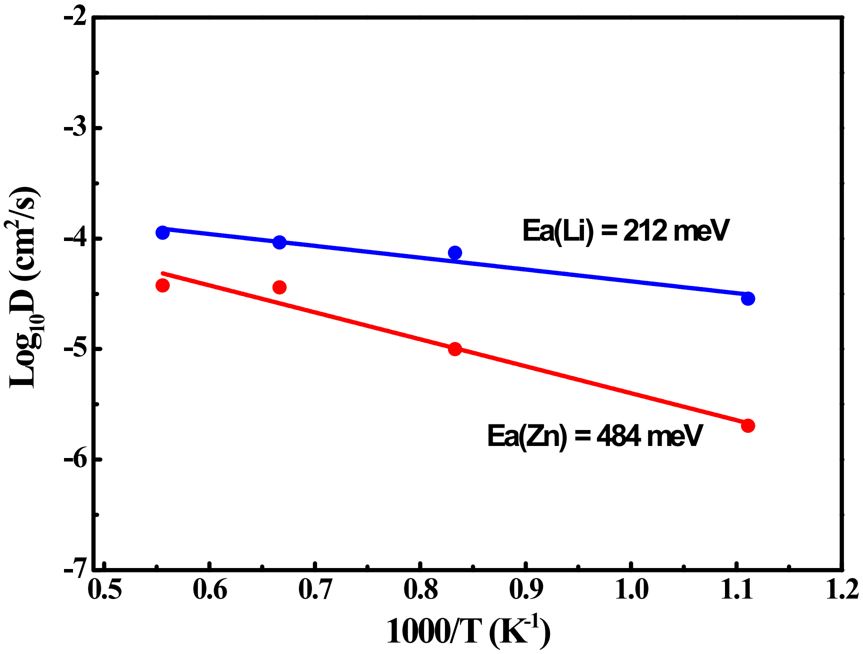

**Figure S21.** Arrhenius plot of electrical conductivities of Li and Zn in the $LiV_2(PO_4)_3$ at various temperatures. Activation energies (Ea) were calculated from the slopes of the fitted lines

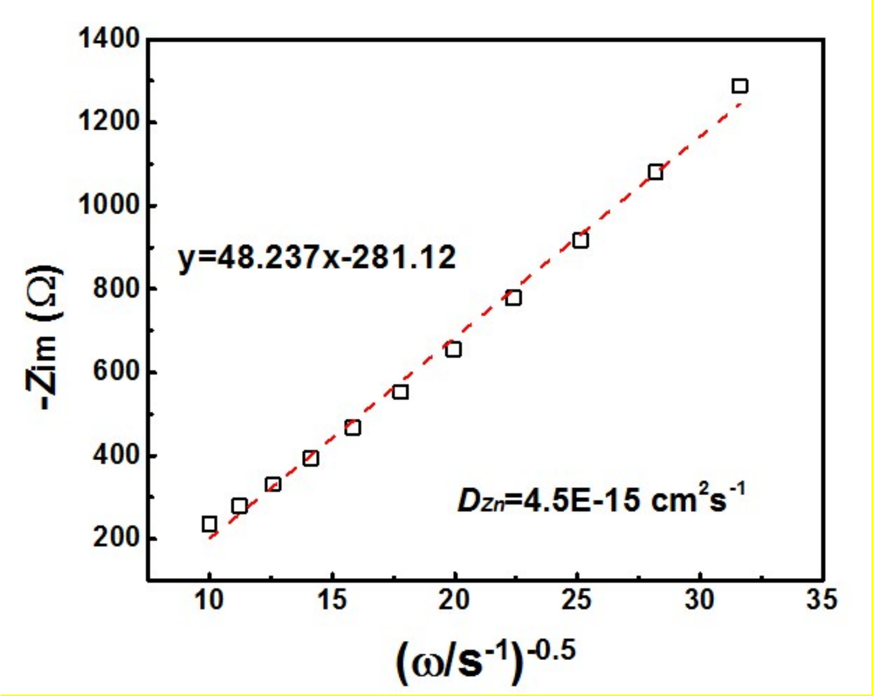

**Figure S22.** The plot of the imaginary resistance versus the inverse square root of angular frequency for $LiV_2(PO_4)_3$ in the Warburg region.(0.01-0.001 Hz) at the first discharging state. The red dashed line corresponds to the linear fitting with the slope marked out.

**Table S2.** The specifications of the Zn/$LiV_2(PO_4)_3$ pouch cell with the dimensions of 300 x 100 x 10 $mm^3$.

| | | |
|---|---|---|
| Cathode<br>($LiV_2(PO_4)_3$) | Reversible capacity | 160 $mAhg^{-1}$ |
| | Voltage | 1.3 V |
| | Composition of active material | 93% |
| | Density (active+conductive+binder) | 2.6 g $cm^{-3}$ |
| | Loading | 20mg $cm^{-2}$ |
| | Swelling | 8% |
| | Thickness (both side coating) | 163 um |
| | Number of stack | 42 |
| Anode<br>(Zinc) | Reversible capacity | 820 $mAhg^{-1}$ |
| | Composition of active material | 100 wt% |
| | Density | 7.14 g $cm^{-3}$ |
| | Loading | 5.8 mg $cm^{-2}$ |
| | Swelling | 0 |
| | Thickness (both side coating) | 16.2um |
| | Number of stack | 43 |
| Full cell | Dimension | 300 x 100 x 10 mm3 |
| | n/p ratio (capacity based) | 1.5 |
| | Total capacity | 74.2 Ah |
| | Voltage | 1.3 V |
| | Energy density | 321Wh $L^{-1}$ |

## References

1 Hammersley, A., Svensson, S., Hanfland, M., Fitch, A. & Hausermann, D. Two-dimensional detector software: from real detector to idealised image or two-theta scan. *High Press. Res.* **14**, 235-248 (1996).

2 Ravel, B. & Newville, M. ATHENA, ARTEMIS, HEPHAESTUS: data analysis for X-ray absorption spectroscopy using IFEFFIT. *J. Synchrotron Radiat.* **12**, 537-541 (2005).

3 Perdew, J. P., Burke, K. & Ernzerhof, M. Generalized gradient approximation made simple. *Physical review letters* 77, 3865 (1996).

4 Hohenberg, P. & Kohn, W. Inhomogeneous electron gas. *Physical review* 136, B864 (1964).

5 Blöchl, P. E. Projector augmented-wave method. *Physical review B* 50, 17953 (1994).

6 Dudarev, S., Botton, G., Savrasov, S., Humphreys, C. & Sutton, A. Electron-energy-loss spectra and the structural stability of nickel oxide: An LSDA+ U study. *Physical Review B* 57, 1505 (1998).

7 Kresse, G. & Hafner, J. Ab initiomolecular-dynamics simulation of the liquid-metal–amorphous-semiconductor transition in germanium. *Physical Review B* 49, 14251-14269, 14251 (1994).

8 Zhu, Z., Chu, I.-H., Deng, Z. & Ong, S. P. Role of Na+ interstitials and dopants in enhancing the Na+ conductivity of the cubic Na3PS4 superionic conductor. *Chemistry of Materials* 27, 8318-8325 (2015).

9 Momma, K. & Izumi, F. VESTA 3 for three-dimensional visualization of crystal, volumetric and morphology data. *Journal of Applied Crystallography* 44, 1272-1276 (2011).